Measurement 264 (2026) 120265

Contents lists available at ScienceDirect

Measurement

journal homepage: www.elsevier.com/locate/measurement

Nonlinear trajectory vehicle tracking system based on distributed magnetic sensors network

Chen Yang, Junqi Gao, Chuancheng Tang, Xiangxiang Zhang, Qiuwei Liu, Lindong Pan, Ying Shen *

National Key Laboratory of Underwater Acoustic Technology, Harbin Engineering University, Harbin 150001, China
Key Laboratory of Marine Information Acquisition and Security (Harbin Engineering University), Ministry of Industry and Information Technology, Harbin 150001, China
College of Underwater Acoustic Engineering, Harbin Engineering University, Harbin 150001, China

ARTICLE INFO

Keywords:
Distributed Magentic sensors
Magnetic anomaly detection

ABSTRACT

This study proposes a novel Grid Search-Particle Swarm Optimization-Strong Tracking Interacting Multiple Model (GS-PSO-ST-IMM) algorithm to address the challenges of tracking vehicles with nonlinear trajectories using distributed magnetic sensor networks. Traditional methods suffer from limited accuracy due to insufficient magnetic moment resolution and motion model mismatch. The key contributions include: (1) integrating geomagnetic background field priors into a hierarchical localization model, refining vehicle position and magnetic moment estimation through grid search and PSO optimization; (2) enhancing tracking robustness by dynamically fusing multiple motion models by Interacting Multiple Model filtering and adjusting filter gains using strong tracking principles to mitigate model mismatch. Simulations demonstrate a 38.7 % reduction in velocity error compared to the Kalman filter, with average localization errors of 0.99 m. Field experiments validate real-time performance, achieving 6.3 % and 8.43 % error ratios under regular and irregular sensor layouts, outperforming centroid and Total Field Matching methods. The framework significantly improves accuracy for complex maneuvers (e.g., sharp steering) while maintaining computational efficiency, offering practical value for security and traffic monitoring applications.

1. Introduction

With the development of Internet of Things (IoT) technology, it has been creating various sensing and monitoring networks based on lots of distributed sensors [1,2]. Particularly, such technique is showing great advantage for the applications of the port security and border monitoring, which require a large volume of sensors [3,4]. As one of important passive detection technologies, magnetic anomaly detection (MAD) has been applied for unexploded ordnance detection, target location, and other areas due to its cross-media detection capability and strong environmental adaptability [5–7]. Previous studies have shown that continuous monitoring of targets, such as ship and vehicle, can be effectively realized by deploying magnetic sensor networks in shallow seabed or open areas, which show great value of enhancing port security and homeland security [8–11].

In fact, IoT technology offers the military an opportunity to monitor vehicle within a specific area through battlefield coverage by thousands of compact magnetic sensors [12]. These remote monitoring sensors can form an unattended ground sensor network to generate magnetic anomaly signals induced by intruding targets, meanwhile, the array configuration is helpful to reduce the false alarm rate. Similarly, in shallow sea monitoring, hundreds of underwater magnetic or acoustic sensors can be deployed to monitor vessels in areas of interest [13,14]. Therefore, it has been drawn lots of interests in the study of a target localization and monitoring by using magnetic sensors [15,16].

Regarding to the issue of vehicle localization by the magnetic sensors, the problem can be described by a nine-dimensional parametric nonlinear optimization problem, which contains the vectors of position, magnetic moment and velocity [17–19]. Generally, current investigations can be divided into two technical routines: one of them is to localize the target based on magnetic vector information. Unfortunately, this type of method is affected greatly by the attitude of vector sensors, as well as errors in the axial direction and observation direction of magnetic sensors. To address these adverse factors, the single-point

* Corresponding author at: Qingdao Graduate School, Harbin Engineering University, Qingdao 266000, China.
E-mail address: shenying@hrbeu.edu.cn (Y. Shen).

https://doi.org/10.1016/j.measurement.2025.120265
Received 25 April 2025; Received in revised form 21 December 2025; Accepted 29 December 2025
Available online 30 December 2025
0263-2241/© 2025 Published by Elsevier Ltd.

gradient methods and tensor methods have been proposed [20–22]. However, these improvements cannot eliminate the errors induced by the intrinsic axial alignment and observation directions of magnetic sensors. Consequently, it imposes extremely high requirements on the layout of sensors. Therefore, vector information-based methods are not suitable for rapidly deployed distributed sensor networks. On the other hand, another important localization strategy is based on magnetic scalar information. In this case, some coefficient fitting approaches, such as the gradient descent and the inverse function methods, have been proposed [23–25]. Nevertheless, the gradient descent method requires reasonable initial solutions and regularly distributed arrays, otherwise, this algorithm is non-convergence. Meanwhile, the performance of the inverse function method is highly dependent on the fitting model, such as the continuity of the objective function, which makes it not reliable. To solve these problems, advanced algorithms like simulated annealing, ant colony and particle swarm optimization have been developed [26–28]. These algorithms are designed to predict the target position by fitting the observed values of magnetic anomaly signals with calculated ones. However, the simulated annealing algorithm requires extensive experiments to select iteration parameters and initial parameters. Although the ant colony algorithm exhibits good performance in local optimization, it is usually intended to be stuck as the parameter space is complicated. Thus, it requires large computational loading and a high number of iterations, which brings in a huge challenge for real-time performance. Meanwhile particle swarm optimization algorithm has been proved to have high accuracy and strong global optimization ability in the field of target location [29,30]. However, there are obvious defects in the response speed and multiplicity in the face of high-dimensional optimization. Furthermore, these algorithms are dealing with the issue of single-point localization. When the target undergoes nonlinear motion, the positioning results between adjacent sensor nodes conflict with each other, leading to a poor target tracking capability. To overcome the limitations of single-point localization, some scholars have adopted array-based approaches, such as the centroid algorithm and the total field matching (TFM) algorithm [31–33]. Most of these methods combine magnetic anomaly signals with geometric weighting methods based on array configurations and estimate motion parameters through spatiotemporal differences in multi-sensor signals. In order to reduce the complexity of computation, these methods normally neglect the dynamic changes of the target's magnetic moment, which limit the prediction accuracy. To address these shortcomings, alternative methods such as least squares and Bayesian filtering have been introduced [34–37]. However, such methods exhibit significant limitations as tracking vehicles with nonlinear motion, such as sharp deceleration, accelerations and lane changes. This unacceptable performance is mainly caused by two unresolved challenges in this research area:

1) Insufficient resolution of magnetic moment parameters. It has been demonstrated that the absence of directional information in the scalar information results in the direct solution encountering multidimensional nonlinear optimization. The conventional algorithms usually take the magnetic moment model as a constant value to reduce the complexity of the solution. However, it should be noted that the positioning accuracy is limited, particularly in the case of localizing the vehicle with nonlinear motion. In this case, the variation of the target's magnetic moment cannot be consistent.

2) Mismatch of the motion models. In order to obtain the parameter of vehicle velocity, an assumption regarding its motion model must be made. Most studies assume that vehicles follow a straight line or make prior decisions based on the direction of the road [38–40]. However, the targets typically exhibit intricate motion patterns, such as lane changing or steering. Consequently, the mismatch between the model assumptions and the actual motions causes the relatively big error as estimating the velocity of target, which directly affects the localization accuracy as well.

Therefore, in order to promote the application of large-scale multi-target monitoring and localization, it is highly desired to derive an advanced algorithm with the great capability of real-time localizing and tracking nonlinearly moving vehicle. In this paper, we propose a Grid Search-Particle Swarm Optimization-Strong Tracking Multi-Model filtering (GS-PSO-ST-IMM) localization and tracking algorithm framework, which is demonstrated to have good performance in this case. The contributions are mainly in the following two aspects: firstly, we introduce the geomagnetic background field into the localization model, which can improve the localization accuracy by considering the effect of background field. Secondly, we track the vehicle by an interactive multi-model filtering tracking framework based on the strong tracking (ST-IMM) filtering. With the help of fusing different motion models, the degradation of localization accuracy caused by the model mismatch can be reduced. More importantly, both simulation and experimental results have shown that our proposed algorithm exhibits higher localization accuracy for nonlinear moving vehicle compared to previous works. Such excellent performance holds it promising for potential applications of developing real-time monitoring system for homeland security, unauthorized vehicle tracking in restricted areas critical and so on.

2. Localization algorithm

The signal processing flowchart of the proposed GS-PSO-ST-IMM localization algorithm is shown in Fig. 1:

Step 1: Identify the abnormal area. According to the amplitudes of magnetic signals captured by the sensors, the area where the target located can be is quickly determined. This area is defined as an abnormal region.

Step 2: (1) Initial localization. The abnormal area obtained from previous step is divided into multiple anchor points, and then an initial solution for the target position and magnitude of magnetic moment can be achieved by searching the one with the smallest error value among the anchor points based the simplified grid search method. Unlike previous works [32–34], it only obtains a rough range for the target position and magnetic moment magnitude in this process. (2) Precise localization. Based on initial solution, the local geomagnetic field is introduced as reference information. Subsequently, a particle swarm optimization algorithm is employed to determine the target position and the magnetic moment precisely. Thus, much more accurate solution can be solved through this new Grid Search-Particle Swarm Optimization (GS- PSO) algorithm.

Step 3: Tracking. In order to predict the nonlinear trajectory of a target, an interactive multi-model filtering tracking framework based on the strong tracking (ST-IMM) concept is proposed. To overcome the limitation of previous work [32], this new method integrates the Kalman filtering with multi-modal filtering and the strong tracking. Benefitting from the dynamic fusion of multiple linear models and adjustment of filter gain, such advanced algorithm is able to track nonlinear targets with sudden changes in motion state. So that, the localization results obtained from Step 2 are used as input to derive the target trajectory through this approach.

2.1. Identify anomaly region

Fig. 2(a) shows the detection layout of a ferromagnetic target moving in a sensor network consisting of multiple groups of sensor nodes. The whole area is divided into different monitoring regions by sensors with different relative positions. We assume that both the target and the sensors are in the same plane, so the position of all the sensors can be uniquely represented by the coordinate system as $P_i(x_i, y_i, z_i)$, and the position of the target can be denoted as $P_m(x_m, y_m, z_m)$.

As a vehicle intrudes into the area covered by the sensor network, it can be a magnetic dipole when the vehicle is far away from the sensor nodes. Therefore, the magnetic anomaly signal $\boldsymbol{B}$ induce by vehicle can be expressed as:

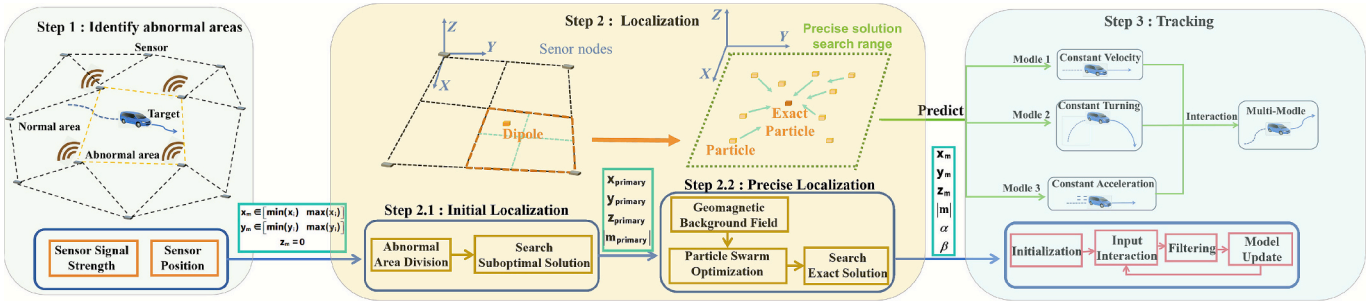

Fig. 1. Signal processing of proposed target localization and tracking method.

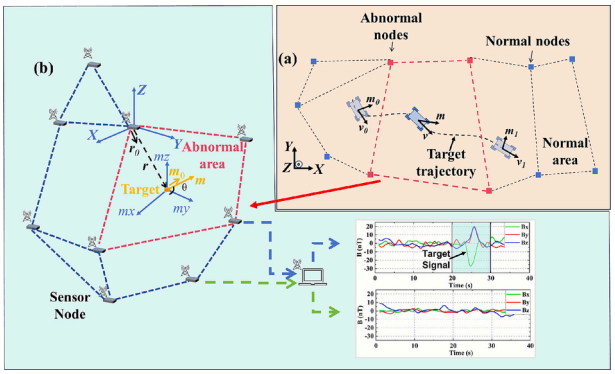

Fig. 2. (a) Target localization by random layout of sensors; and (b) Model diagram of magnetic anomaly detection.

$$\boldsymbol{B} = \frac{\mu_0}{4\pi}\left[\frac{3(\boldsymbol{m}\bullet\boldsymbol{r})\boldsymbol{r}}{|\boldsymbol{r}|^5} - \frac{\boldsymbol{m}}{|\boldsymbol{r}|^3}\right] \tag{1}$$

where μ_0 is the vacuum permeability, which is equal to $4\pi \times 10^{-7} H/\mathrm{m}$. $\boldsymbol{r}$ denotes the relative position vector of the sensor and the magnetic dipole, and $\boldsymbol{m}$ denotes the magnetic moment of the vehicle.

According to the configuration of a magnetic dipole model shown in Fig. 2(b), the Eq. (1) can be rewritten as:

$$|\boldsymbol{B}| = \frac{1}{|\boldsymbol{r}|^3}\frac{\mu_0|\boldsymbol{m}|}{4\pi}|3\boldsymbol{r}_0\cos\theta - \boldsymbol{m}_0| \tag{2}$$

where $\boldsymbol{m}_0$ denotes a unit vector of the magnetic moment of the magnetic dipole, $\boldsymbol{r}_0$ denotes a unit vector of the relative position of the sensor and the magnetic dipole, and θ denotes the angle between $\boldsymbol{m}$ and $\boldsymbol{r}$.

Thus, the total field signal induced by the magnetic dipole can be expressed as:

$$|\boldsymbol{B}| = \frac{\mu_0|\boldsymbol{m}|}{4\pi}\frac{1}{|\boldsymbol{r}|^3}\rho \tag{3}$$

where $\rho = |3\boldsymbol{r}_0\cos\theta - \boldsymbol{m}_0|$.

The value of ρ depends on the relative position between the vehicle and the sensor and the direction of the magnetic moment. That is, it is determined by the position of the vehicle and the direction of the magnetic moment, but it cannot be obtained through priori knowledge. However, according to θ satisfies $0^\circ \le \theta < 360^\circ$, it is derived that ρ can be determined to be from 1 to 2.

According to Eq. (3), the magnitude of the signal received by sensors is mainly determined by the distance between the magnetic dipole and sensors. Therefore, the position of the dipole is locked in the region enclosed by these N sensors that receive the maximum signal magnitude. Therefore, the position of the magnetic dipole satisfies $xm \in [\min(xi), \max(xi)]$, $y_m \in [\min(y_i), \max(y_i)]$, where x_i, y_i denote the relative coordinates of the i-th node in the sensor network.

2.2. Localization

The localization issue for a magnetic target can be described as a six-variable optimization problem involving the target position and magnetic moment. According to previous results [41,42] the magnetic moment direction is significant changed as the target undergoes nonlinear motion. Therefore, a real-time calculation of magnetic moment is critical for positioning nonlinear moving target. To avoid falling into local optimal solution and excessive computation time when directly solving for target location and magnetic moment, we firstly approximate the target position and magnetic moment magnitude by ignoring the magnetic moment direction [32–34,43]. Subsequently, based on this approximate solution, we redefine the search space and incorporate magnetic moment direction information to perform precise calculations. The directional information of the magnetic moment was determined through stepwise positioning. This approach can achieve higher positioning accuracy in nonlinear motion localization.

2.2.1. Initial localization

Based on Eq. (3), the magnitude of the magnetic moment of the magnetic dipole can be expressed as:

$$|\boldsymbol{m}| = 4\pi\frac{|\boldsymbol{B}||\boldsymbol{r}|^3}{\rho\mu_0} \tag{4}$$

According to Eq. (4), the amplitude of the magnetic moment for the target is unique. Therefore, instead of calculating the target position by using Eq. (3), the error function (Eq. (5)) is established to describe the mismatch between the true magnetic moment value of the magnetic dipole and the estimated value by using our proposed algorithm. So, the problem of localization is transformed into finding the minimum value of the error function.

$$e(\Delta\boldsymbol{m}) = \sqrt{\sum_{i=1}^{N}\left(|\boldsymbol{m}_i| - \frac{1}{N}\sum_{i=1}^{N}|\boldsymbol{m}_i|\right)^2} \tag{5}$$

where $|\boldsymbol{m}_i|$ denotes the amplitude of the vehicle magnetic moment obtained by the magnetic signal from the i-th sensor among the N sensors in this anomaly region.

In detail, according to the definition of error function, it can be noticed that the smaller the value of the error function, the closer estimated position to the real vehicle position. Therefore, the grid coordinates corresponding to the value of $\min(e(\Delta\boldsymbol{m}))$ is regarded as the primary location of the vehicle. It should be noted that the ρ value involves multi-dimensional parameter coupling. It mainly includes the relative positions of the sensor and the vehicle, the geomagnetic field environment characteristics, the 3D configuration of the vehicle and the platform attitude angle, and other influencing factors. If solved directly it will face high-dimensional nonlinear optimisation. Most of the previous research simplify the positioning model by simplifying the influence of ρ according to the small range variation of $\rho \in [1,2]$. such as the centre point positioning algorithm, the Total Field Matching (TFM)

algorithm [32,33,44]. In order to avoid high-dimensional nonlinear optimisation, we take $\rho = 1.4$ to simplify the model to obtain the vehicle position and magnetic moment initial solutions according to previous results. However, one should be noted that this process only obtains an initial solution for the target position and magnetic moment, rather than directly deriving the localization of target.

As shown in Fig. 3(a), for the characteristics of the magnetic anomaly region, we adopt a grid deployment strategy to construct an array of anchor points. By constructing the error evaluation function based on Eq. (5), the magnetic moment matching degree is calculated for each anchor point, and the spatial coordinates corresponding to the minimum error value are finally selected as the initial localization solution of the target vehicle, and the magnetic moment inversion is completed simultaneously. It should be particularly pointed out that the mathematical properties of Eqs. (4)-(5) indicate that this error function presents significant spatial heterogeneity characteristics in the solution space. In order to optimize the allocation of computational resources, this scheme designs a multilevel grid refinement strategy: as shown in Fig. 3(b), by constructing a progressive anchor distribution architecture from sparse to dense, and adopting an iterative mechanism of step-by-step convergence, we can effectively reduce the load of a single operation while guaranteeing the positioning accuracy, so as to achieve a dynamic balance between computational efficiency and positioning accuracy.

2.2.2. *Precise localization*

In the rough localization phase, we can obtain initial estimates of the vehicle position and magnetic moment strength $\left(x_{primary}, y_{primary}, |\boldsymbol{m}_{primary}|\right)$. However, due to the parameter simplification strategy, the process inevitably introduces systematic errors. In order to accurately solve the magnetic moment direction, we introduce a system of direction parameters based on the initial solution: let α be the angle between the magnetic moment vector and the vertical direction ($0^\circ < \alpha < 180^\circ$), and β be the angle between the horizontal projection of the magnetic moment and the due-east direction ($0^\circ < \beta < 360^\circ$), and thus construct a complete representation of the magnetic moment vector:

$$B_{iEast} = \frac{\mu_0}{4\pi r^3}\left[3(x_{PSO}-1)m_{East} + 3x_{PSO}y_{PSO}m_{North} + 3x_{PSO}z_{PSO}m_{Vertical}\right] \quad (6)$$

$$B_{iNorth} = \frac{\mu_0}{4\pi r^3}\left[3x_{PSO}y_{PSO}m_{East} + 3(y_{PSO}-1)m_{North} + 3y_{PSO}z_{PSO}m_{Vertical}\right] \quad (7)$$

$$B_{iVertical} = \frac{\mu_0}{4\pi r^3}\left[3x_{PSO}z_{PSO}m_{East} + 3y_{PSO}z_{PSO}m_{North} + 3(z_{PSO}-1)m_{Vertical}\right] \quad (8)$$

where $\left(x_{PSO}, y_{PSO}, |\boldsymbol{m}_{PSO}|\right)$ denotes the PSO algorithm particle constructed based on the results obtained from the coarse localization. $m_{East}, m_{North}, m_{Vertical}$ denotes the component of the magnetic moment in the east, north and vertical directions which can be obtained from the orthogonal decomposition of $|\boldsymbol{m}_{PSO}|$, α and β. $B_{iEast}, B_{iNorth}, B_{iVertical}$ represents magnetic field generated by the vehicle in the east direction, the north direction and the vertical direction.

According to working principle, the magnetic sensor measures the projected component of the magnetic field along the geomagnetic background direction. Thus, the magnetic field signals received by different sensors inside the anomaly region are not only various in intensity, but also in their projection directions relative to the geomagnetic field. Considering that the geomagnetic background strength $\boldsymbol{B}_g$ and its direction parameters (magnetic inclination φ, magnetic declination γ) can be accurately obtained by a regional geomagnetic model, they are taken as a priori constraints in this study. The strength and direction characteristics of the observed signals are jointly determined by three sets of parameters: 1) the position coordinates (x_m, y_m) and the magnetic moment modulus $\boldsymbol{m}$ of the target vehicle. 2) the magnetic moment direction parameters (α, β). 3) the geomagnetic field background direction (φ, γ).

Parameter 1) can be coarsely located to obtain an estimate as an initial solution, and parameter 3) can be directly called from the Geographic Information System database. So, we implement the global spatial search for parameter 2, while the neighbourhood local adjustment for parameter 1. In order to achieve multi-parameter collaborative optimisation, PSO algorithm is used to solve the problem:

As the magnetic moment and the position of the target is determined,

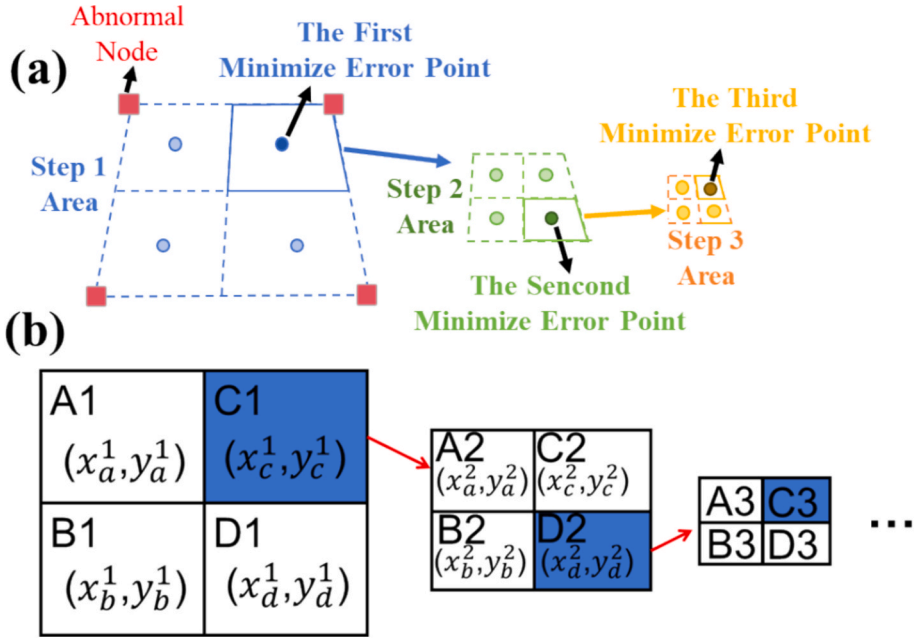

Fig. 3. (a) Schematic diagram of anchor division (b) Schematic diagram of distribution anchor division.

the magnetic anomaly signal received by the i-th sensor can be found to be B_i according to Eq. (2), and the signal B received by the sensor can be described as:

$$B_i = \sqrt{\left(B_{\text{gEast}} + B_{\text{iEast}}\right)^2 + \left(B_{\text{gNorth}} + B_{\text{iNorth}}\right)^2 + \left(B_{\text{gVertical}} + B_{\text{iVertical}}\right)^2} \quad (9)$$

where B_{gEast},B_{gNorth},$B_{gVertical}$ denotes the strength of the geomagnetic background in the due east, due north and vertical directions. These can be calculated from magnetic declination and inclination angles.

Based on Eq. (9) it is possible to determine an error function as an adaptation function for the PSO algorithm:

$$e_{\text{m}} = \sum_{i=1}^{N} \left(\left|\boldsymbol{B}_{pos}\right| - \left|\boldsymbol{B}_i\right|\right)^2 \quad (10)$$

where $|\boldsymbol{B}_i|$ is the actual observed value of i-th sensor. $|\boldsymbol{B}_{pos}|$ denotes the observation of i-th sensor inverted from the parameters of the current particle by Eq. (1).

In terms of parameter optimization configurations, the spatial boundary conditions of the parameters in the PSO algorithm involving the vehicle position coordinates (x_{PSO}, y_{PSO}) and the magnetic moment modulus $\boldsymbol{m}_{PSO}$ will be systematically elaborated in the localization simulation in Chapter 3.

By using our proposed 2-steps GS-PSO localization strategy, the positioning accuracy of nonlinearly moving vehicles can be enhanced greatly. Specifically, with the help of introducing the geomagnetic background field into the positioning algorithm, the issue such as falling into local optimal solution caused by a direct six degree-of-freedom nonlinear optimization can be avoided effectively.

2.3. Tracking

To address the inversion problem of vehicle kinematic parameters (v_x, v_y, v_z), we recursively estimate the target localization points obtained from the localization algorithms through the filtering system based on the dynamic system equations and the magnetic dipole observation model. An in-depth analysis reveals that the traditional Kalman filter (KF) and its extended form (EKF) can achieve motion state tracking through a linear approach though. However, due to the inherent defects of a single motion model, the tracking accuracy will be degraded due to model mismatch when the vehicle has nonlinear motion patterns such as sharp steering. To address this problem, we achieve adaptive fusion of motion models through the IMM architecture by adopting a multi-model fusion mechanism in time-varying motion modes. We also introduce the strong tracking idea and obtained the ST-IMM, which improves the sensitivity of the filtering algorithm to sudden changes in the motion state by dynamically adjusting the filtering gain in the filtering algorithm.

As shown in Fig. 4, the ST-IMM filter is based on the IMM filter, where a fading factor λ is introduced for each model in IMM filter, and the filtered model gain is increased by the fading factor when the model does not satisfy orthogonality in order to improve model tracking. For example, as the target undergoes a sudden change in motion state, the filtering gain would be rapidly increased through the factor of λ, which can enhance the tracking accuracy. The filtering process can be represented as the following steps:

(i) Initialization

Considering there are a total of r motion models with two observation time intervals of ΔT under different models j, the motion state of the vehicle under $k\Delta T$ moments can be expressed as $s_j(k)$:

$$s_j(k) = \begin{bmatrix} x_m(k) & v_x(k) & y_m(k) & v_y(k) & a_x(k) & a_y(k) \end{bmatrix}^T \quad (11)$$

where $[x_m(k) \quad y_m(k)]$, $[v_x(k) \quad v_y(k)]$, $[a_x(k) \quad a_y(k)]$ denotes the position, velocity and acceleration information of the vehicle at moment $k\Delta T$, respectively. Therefore, the measurement equation at moment $k\Delta T$ can be expressed as:

$$Z_j(k) = H_j s_j(k) + N_j(k) \quad (12)$$

where $N_j(k)$ denotes the total noise caused by the sensor intrinsic noise and environmental noise; H denotes the corresponding state transfer matrix of the vehicle at the moment $k\Delta T$, which represents the relationship between the measured position and the true position. H can be expressed as:

$$H = \begin{bmatrix} 1 & 0 & 0 & 0 & 0 & 0 \\ 0 & 0 & 1 & 0 & 0 & 0 \end{bmatrix} \quad (13)$$

The corresponding equations of state for different motion models can be expressed as:

$$s_j(k/k-1) = A_j s_j(k-1) + W_j(k) \quad (14)$$

where $W_j(k)$ denotes the process noise; A_j denotes the prediction matrix under different model j, and different motion models correspond to different prediction matrices. For example, the prediction matrices of constant velocity (CV) model, constant turning (CT) model and constant

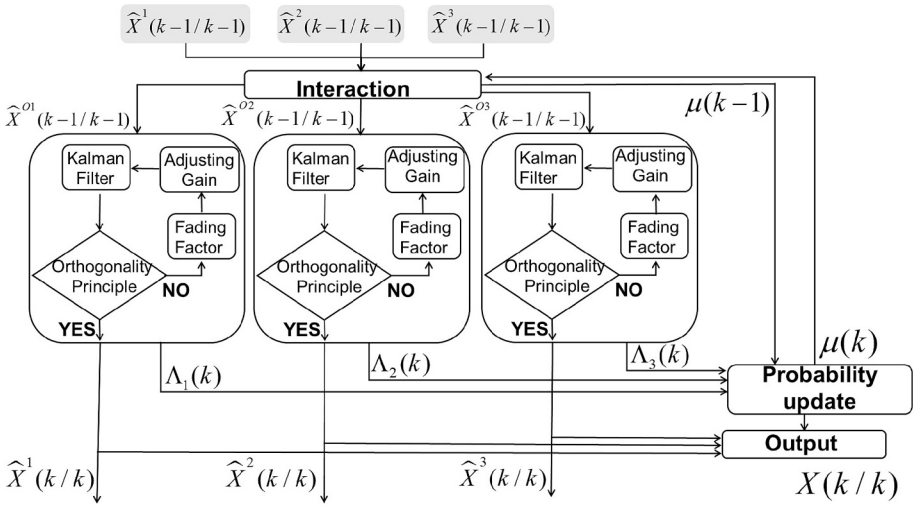

Fig. 4. ST-IMM Flowchart.

acceleration (CA) model can be expressed as:

$$A_{CV}=\begin{bmatrix}1&\Delta t&0&0&0&0\\0&1&0&0&0&0\\0&0&1&\Delta t&0&0\\0&0&0&1&0&0\\0&0&0&0&0&0\\0&0&0&0&0&0\end{bmatrix} \tag{15}$$

$$A_{CT}=\begin{bmatrix}1&\sin(\omega\Delta t)/\omega&0&-(1-\cos(\omega\Delta t))/\omega&0&0\\0&\cos(\omega\Delta t)&0&-\sin(\omega\Delta t)&0&0\\0&(1-\cos(\omega\Delta t))/\omega&1&\sin(\omega\Delta t)/\omega&0&0\\0&\sin(\omega\Delta t)&0&\cos(\omega\Delta t)&0&0\\0&0&0&0&0&0\\0&0&0&0&0&0\end{bmatrix} \tag{16}$$

$$A_{CA}=\begin{bmatrix}1&\Delta t&0&0&\Delta t^2/2&0\\0&1&0&0&\Delta t&0\\0&0&1&\Delta t&0&\Delta t^2/2\\0&0&0&1&0&\Delta t\\0&0&0&0&1&0\\0&0&0&0&0&1\end{bmatrix} \tag{17}$$

These three models can describe the most common status of vehicle motion. The prediction model can avoid the tracking inaccuracy caused by model mismatch effectively as the fusion of three models expressed by Eqs. (15)-(17). The transfer between the models is determined by a Markovian probability transfer matrix:

$$P=\begin{bmatrix}p_{11}&\cdots&p_{1r}\\ \cdots&\cdots&\cdots\\ p_{r1}&\cdots&p_{rr}\end{bmatrix} \tag{18}$$

where p_{ij} denotes the probability of the vehicle transferred from the i-th motion model to the j-th motion model. In this paper P takes the value:

$$P=\begin{bmatrix}0.95&0.025&0.025\\0.025&0.95&0.025\\0.025&0.025&0.95\end{bmatrix} \tag{19}$$

(ii) Input Interaction

The mixed estimate $\hat{s}_{oj}(k-1/k-1)$ and covariance $P_{oj}(k-1/k-1)$ are obtained from the state estimate $\hat{s}_j(k-1/k-1)$ at the vehicle $(k-1)\Delta T$ moment and the model probability $u_j(k-1)$ for each filter, treating the mixed estimate as the initial state of the current loop. The expression is given below:

$$\bar{c}_j=\sum_{i=1}^{r}p_{ij}u_i(k-1) \tag{20}$$

$$u_{ij}(k-1/k-1)=\frac{1}{\bar{c}_j}\sum_{i=1}^{r}p_{ij}u_i(k-1) \tag{21}$$

$$\hat{s}_{oj}(k-1/k-1)=\sum_{i=1}^{r}\hat{X}_i(k-1/k-1)u_{ij}(k-1/k-1) \tag{22}$$

$$P_{oj}(k-1/k-1)=\sum_{i=1}^{r}\begin{matrix}u_{ij}(k-1/k-1)\{P_i(k-1/k-1)+\\ \left[\hat{s}_i(k-1/k-1)-\hat{s}_{oj}(k-1/k-1)\right]\bullet\\ \left[\hat{s}_i(k-1/k-1)-\hat{s}_{oj}(k-1/k-1)\right]^T\}\end{matrix} \tag{23}$$

where $\bar{c}_j$ denotes the predicted probability of model j, $u_{ij}(k-1/k-1)$ denotes the mixing probability from model i to j. In order to improve the robustness of the algorithm, we give higher probabilities to the more general models at the initial stage, with initial probabilities of 0.7, 0.15, and 0.15 for the CV, CT, and CA models, respectively.

(iii) Strong Tracking KF (model j)

As mentioned above, a strong tracking refers to a strategy that directly modulates filtering gain through additional factors.

KF uses a posteriori state estimate $\hat{s}_{oj}(k-1/k-1)$, the filter covariance $P_{oj}(k-1/k-1)$, and the measurement location $Z(k)$ at moment k-1 as the inputs for filtering to update the prediction of the state $\hat{s}_j(k/k)$ and the filter covariance $P_j(k/k)$ at the moment k. The expression is given below:

$$\hat{s}_j(k/k-1)=A_j\hat{s}_{oj}(k-1/k-1) \tag{24}$$

$$P_j(k/k-1)=A_jP_{oj}(k-1/k-1)A_j^T+Q_j \tag{25}$$

$$K_j(k)=P_j(k/k-1)H\left(HP_j(k/k-1)H^T+R\right)^{-1} \tag{26}$$

$$\hat{s}_j(k/k)=\hat{s}_j(k/k-1)+K_j(k)\left(Z(k)-Hs_j(k/k-1)\right) \tag{27}$$

$$P_j(k/k)=\left(I-K_j(k)H\right)P_j(k/k-1) \tag{28}$$

where $K_j(k)$ denotes the gain of the filter.

The strong tracking Kalman is based on (27) and satisfies the orthogonal principle:

$$E\left[\left(s_j(k)-\hat{s}_j(k)\right)\left(s_j(k)-\hat{s}_j(k)\right)^T\right]=\min \tag{29}$$

$$E\left[\left(Z_j(k+i)-H_j\hat{s}_j(k+i/k+i-1)\right)\left(Z_j(k)-H_j\hat{s}_j(k/k-1)\right)^T\right]=0,i=1,2.. \tag{30}$$

In fact, the filtering and tracking process is essential to minimize the state residual. When both of the above indicators described by Eqs. (29) and (30) are satisfied, the output residual of the filter becomes an uncorrelated Gaussian white noise sequence. At this condition, the hybrid motion model of the filter matches the real motion model, resulting an optimal tracking performance. Also, introduce the decay factor $\lambda_j(k)$ and rewrite (25) as:

$$P_j(k/k-1)=\lambda_j(k-1)A_jP_{oj}(k-1/k-1)A_j^T+Q_j \tag{31}$$

where $\lambda_j(k)=diag*\left(\lambda_{1j}(k),\lambda_{nj}(k)...,\lambda_{nj}(k)\right)$, $\lambda_{ij}(k)$ can be expressed as:

$$\lambda_{ij}(k)=\begin{cases}\lambda_0 & ,\lambda_0>1\\ 1 & ,\lambda_0\le 1\end{cases}\quad i=1,2...,n \tag{32}$$

$$\lambda_0=\frac{tr\left[V_0(k+1)-bR(k+1)-HQ_jH^T\right]}{tr[M(k+1)]} \tag{33}$$

$$V_0(k)=\begin{cases}\left(s_j(0)-\hat{s}_j(0)\right)\left(s_j(0)-\hat{s}_j(0)\right)^T & ,k=1\\ \dfrac{rV_0(k-1)+\left(s_j(0)-\hat{s}_j(0)\right)\left(s_j(0)-\hat{s}_j(0)\right)^T}{1+r} & ,k>1\\ & 0\le r<1\end{cases} \tag{34}$$

where r denotes the forgetting factor, and b denotes the weakening factor. Considering that the actual non-linear motion state of the vehicle mainly includes steering, acceleration, etc., we take $r=0.95$ and $b=0.3$ [45,46].

When the factor of $V_0(k)$ is increased due to an abrupt change in the vehicle's motion state the filter gain of $K_j(k)$ is also increased accordingly. So that, the tracking ability is enhanced as performing this process.

(iv) Model probability update

The model probability $u_j(k)$ is updated by calculating the likelihood function with the following expression:

$$\Lambda_j(k)=\frac{1}{\sqrt{(2\pi)^n|S_j(k)|}}\exp\left\{-\frac{1}{2}d_j^T(k)S_j^{-1}(k)d_j(k)\right\} \tag{35}$$

$$u_j(k)=\frac{1}{\sum_{j=1}^{r}\Lambda_j(k)\bar{c}_j}\Lambda_j(k)\bar{c}_j \tag{36}$$

where $S_j(k) = HP_j(k/k-1)H^T + R$, $d_j(k) = Z(k) - H\hat{s}_j(k/k-1)$.

Instead, the filtering results simply combine the state estimates $\hat{s}(k/k)$ and covariance estimates $P(k/k)$ from the different models weighted by the model probabilities.

$$\hat{s}(k/k) = \sum_{j=1}^{r} \hat{s}_j(k/k)u_j(k) \tag{37}$$

$$P(k/k) = \sum_{j=1}^{r} u_j(k)\{P_j(k/k) + [\hat{s}_j(k) - \hat{X}(k/k) \bullet [\hat{s}_j(k) - \hat{X}(k/k)]^T\}] \tag{38}$$

In summary, we localize the vehicle position and magnetic moment by GS-PSO and then track the vehicle by ST-IMM based on the GS-PSO results.

3. Simulation

To demonstrate the proposed localization algorithm, a simulation is performed. As shown in Fig. 5(a), 36 magnetic sensors are randomly distributed in an area of 10000 m^2. The target motion path is divided into two stages: the first stage is accelerated linear motion with an initial velocity of 1 m/s with acceleration of 1 m/s^2, and the second one is a constant circular motion with a radius of 30 m with an angular velocity of $(\pi/60)\,rad/s$. Furthermore, the magnetic moment of the target $|\boldsymbol{m}| = 1000\,A{\cdot}m^2$, and the orientation of the magnetic moment is set up at an angle of 90° to the Z-axis and 60° to the X-axis. The background magnetic field is 53,000 nT with a magnetic inclination of −7.3° and a magnetic declination of 53°. A 10 % Gaussian white magnetic noise was used in the calculations, and the detection threshold is 10nT.

The distance between the localization points and the real position of the vehicle obtained by the above algorithm and ST-IMM filtering is used as the error.

$$error_L = \sqrt{(x_m - x_L)^2 + (y_m - y_L)^2 + (z_m - z_L)^2} \tag{39}$$

$$error_T = \sqrt{(x_m - x_T)^2 + (y_m - y_T)^2 + (z_m - z_T)^2} \tag{40}$$

where $P_L(x_L, y_L, z_L)$ denotes the target position obtained by the localization algorithm and $P_T(x_T, y_T, z_T)$ denotes the target position obtained by ST-IMM filtering. The error is calculated based on the results obtained from localization and the results after localization filtering, respectively.

Meanwhile, the area D_{avg} of the average distance of each sensor from neighbouring sensors can be obtained based on the ratio of the area S_{sensor} covered by the sensor array to the number of sensors Num_{sensor} in the sensor array:

$$D_{\text{avg}} = \sqrt{\frac{S_{\text{sensor}}}{Num_{sensor}}} \tag{41}$$

In this simulation, D_{avg} is 16.67 m.

Therefore, to evaluate the localization error relative to the array scale, we define a dimensionless ratio M as the ratio of the localization error to D_{avg}:

$$M = \frac{error}{D_{avg}} \tag{42}$$

where *error* is the localization error (in meters), and D_{avg} is the characteristic length of the array. M quantifies the relative error, enabling fair comparison across arrays of different sizes.

According to Eq. (4), the magnetic moment magnitude of the target can be inverted by bringing in the localization results. Thus, again the accuracy of the magnetic moment prediction can be reacted by the parameter D_m.

$$D_m = \frac{|\boldsymbol{m}_{est}| - |\boldsymbol{m}|}{|\boldsymbol{m}|} \tag{43}$$

where $\boldsymbol{m}_{\text{est}}$ denotes the inverted target magnetic moment magnitude and $\boldsymbol{m}$ denotes the true magnetic moment magnitude.

To determine the search area in the PSO algorithm, we randomly distribute four sensors in a 20 × 20 m^2 area targeting dipole targets of 50–500 A·m^2. A rough localization of this dipole target is performed using a grid search method in the absence of noise background. The simulation is repeated 50,000 times, and the error of each localization is counted as well as the error of the magnitude of the backpropagated magnetic moment. The results are shown in Fig. 6.

In the statistical results, we separately seek the results of 99 % of the distributions in the vicinity of 0 in 50,000 sets of simulations as the solution region of the PSO algorithm:

$$x_{PSO} \in \left[x_{primary} - Distance \times D_{xy}, x_{primary} + Distance \times D_{xy}\right] \tag{44}$$

$$y_{PSO} \in \left[y_{primary} - Distance \times D_{xy}, y_{primary} + Distance \times D_{xy}\right] \tag{45}$$

$$|\boldsymbol{m}_{PSO}| \in [|\boldsymbol{m}_{primary}| \times (\mathbf{1} - D_{mUL}), |\boldsymbol{m}_{primary}| \times (\mathbf{1} + D_{mLL})] \tag{46}$$

where *Distance* denotes the average neighbouring sensor spacing, D_{xy} = 11.7 % represents the proportion of distance error, D_{mUL} = 22.3 % and D_{mLL} = -29.8 % represent the upper and lower limits of magnetic moment error.

The target tracking results are shown in Fig. 6(a) the red line indicates the real moving path of the target, and the localization points obtained by GS-PSO method are marked as green squares. Moreover, the path obtained by traditional linear KF is indicated as blue triangles, and the path obtained by our proposed ST-IMM filtering is marked as yellow triangles. From this figure, it can be found that as the motion parameters of the target are changed, the tracking error based on the normal KF method is relatively large as expected. However, benefitting from the ST-IMM algorithm, the tracking error can be eliminated greatly. Thus, the predicated path is quite close to the real one.

Moreover, the errors of the target localization in this case are also analysed by calculating the mismatched values between the estimated positions and the real ones. As shown in Fig. 5(b), for almost all of moving process, the tracking errors based on KF is obviously greater than the values of the ST-IMM filtering. Especially for the time around 17 s, when the motion of the target is changed from the linear acceleration to the circular speed, the estimated position by using KF is dramatically increased to over 6 m. That is unacceptable for the tracking in the real application. As a comparison, the ST-IMM filtering method shows much better performance in this situation, which can keep the error value around 2 m. Statistically, the average error of the localization trajectory based on the total field matching search is around 1.09 m with variance of 0.34, M is 5.76 %. After applying the KF, these values are increased to 1.65 m and 0.72, M is 8.24 %, respectively, which means this method brings more uncertainty. The ST-IMM filtering can bring these numbers down to 0.99 m with variance of 0.29, M is 5.17 %. These results have been also demonstrated that the ST-IMM filtering works much more efficiency for tracking the target with more complicated motion.

Fig. 5(c) shows the error comparison results of predicting the target motion state using KF and ST-IMM algorithms, respectively, after obtaining the localization coordinates based on the GS-PSO localization algorithm The results. The error curve analysis shows that the ST-IMM algorithm has a significant advantage over the traditional KF in terms of trajectory tracking accuracy. Especially at the critical stage when the target undergoes manoeuvre steering, the ST-IMM algorithm shows stronger adaptive ability, and its dynamic error amplitude is reduced by about 38.7 % compared with the KF. It is worth noting that the KF algorithm shows an obvious hysteresis effect when the heading changes

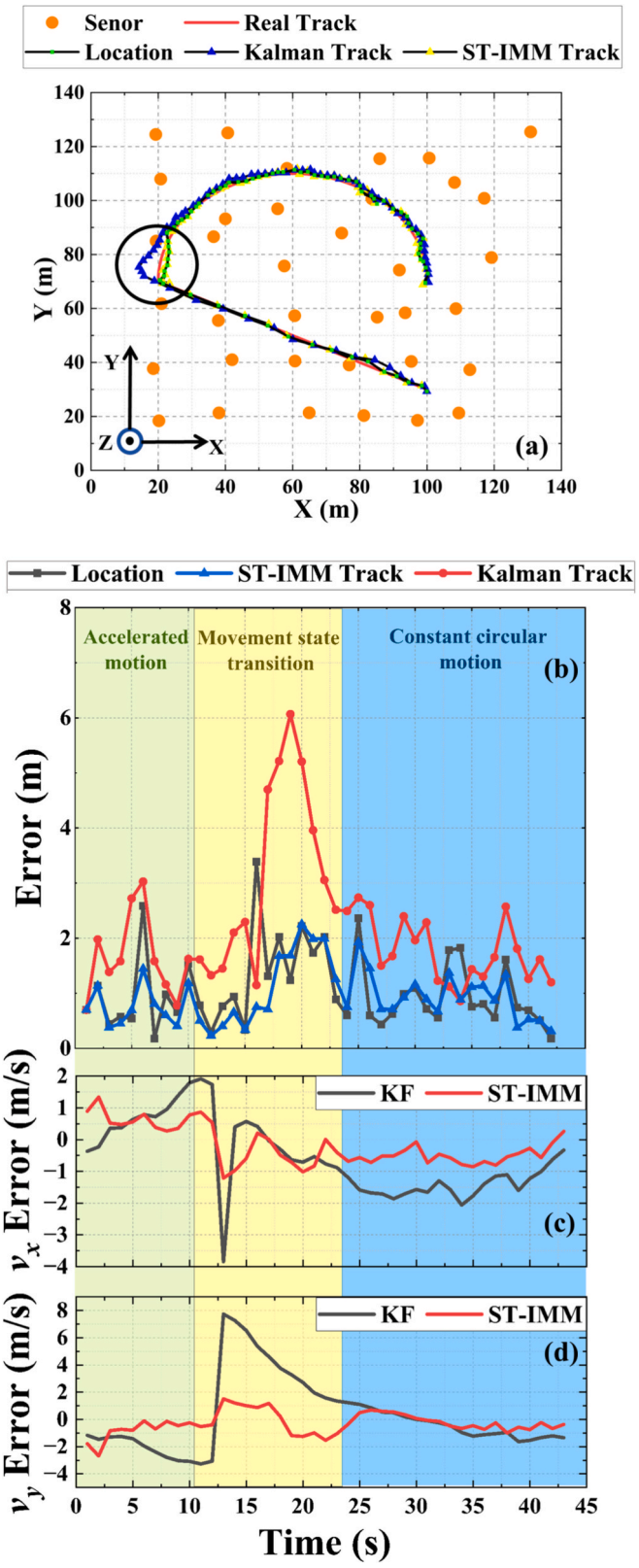

Fig. 5. (a) Localization and tracking trajectories of the target in a monitoring area of 120 m*120 m. (b) Localization error on the target and tracking error after filtering with two filters. (c)(d) Velocity errors obtained from KF and ST-IMM.

abruptly, and it needs 5–8 sampling cycles of convergence to reach a stable tracking state again, whereas the ST-IMM algorithm can shorten the convergence time to 2–3 sampling cycles through the model probability self-adaptive adjustment mechanism.

4. Experiment in field

In order to demonstrate our proposed algorithm, the vehicle localization experiment was performed in the real environment field. During the test, ten magnetic sensor nodes were placed in this area. Each of such nodes consist of a 3-axis Tunnelling Magnetoresistance (TMR) sensor (TMR9082, MultiDimension Technology Co., Ltd, China). The sensitivity of this sensor is 3.5 V/Oe with intrinsic magnetic noise of 250pT/rtHz at 1 Hz. Moreover, a 50 Hz low-pass filter circuit is designed to filter out high-frequency noise. An ADC circuit converts the magnetic signal received by the TMR sensor into a digital signal with a sampling rate of 20 Hz. And then, the digital signals are transmitted to the host computer for processing by wireless transmission module.

According to previous study [47], the upper limit frequency of the target magnetic anomaly signal is related to the minimum distance closest point of approach (CPA) between the target and the sensor, and the velocity of target v. It can be described by the following equation:

$$f \approx 0.85 \frac{v}{CPA} \tag{47}$$

where f represents the upper limit frequency of the signal.

Considering our study of vehicle localization, the sampling rate of 20 Hz is sufficient for capturing the MAD signals.

Fig. 7(a), (b) illustrates the distribution of the sensors: the distance between two sensors is around 20 m. The experimental site is located at a park in Qingdao, China, where the environmental magnetic field noise is about 1 nT. As shown in Fig. 7(c), (d), the sensors of No. 1~9 were classified into two types of placements: one is rectangular array, and the other is random array. At the same time, the No. 10 sensor was placed near the array as a reference point to reject the effect of geomagnetic fluctuations during the detection. The number of alarm sensors N was selected as 4 and the detection threshold is 10 nT.

Fig. 8(a) shows a section of original measured data obtained from the TMR sensor: it can be found that there are different degrees of electromagnetic interference (EMI) for all three axes of sensor which is mainly caused by wireless transmission module. In detail, this EMI noise shows obvious periodicity in time domain, which is consistent with the transmission period of wireless digital transmission, and the frequency partially overlaps with the signal frequency. Therefore, wave packet decomposition with high time–frequency resolution is selected to eliminate EMI in time domain. Due to the strict requirements of the localization algorithm on the phase characteristics of the signal, the " sym" wavelet with approximate symmetry is selected here [48,49]. At the same time, in order to ensure computational efficiency, the " sym4" wavelet with a support length of 8 is selected to decompose the signal [50]. The layers with entropy values larger than the threshold are rounded off and the signal is reconstructed. The filtered result is shown in Fig. 8(b); it can be seen the signal can effectively filter out the EMI caused by wireless digital transmission and ensure the strict phase characteristic.

The travelling trajectory of the target vehicle in the sensor array was localized by using the Real-Time Kinematic (RTK) system, which has a localization error of less than 10 cm. So, this measured position is used for the real path of the vehicle, vehicles moved for 19 s in the regular array and 23 s in the irregular array. The results of localization trajectories are shown in Fig. 9(a), (b): The red curves indicate the trajectories localized by the GS-PSO algorithm and tracked by the ST-IMM filter, the green ones indicate the results obtained by the TFM algorithm, and the purple ones indicate the results obtained by the Centroid Localization algorithm. According to the trajectory, it can be found intuitively that the Centroid Localization algorithm has the lowest positioning accuracy,

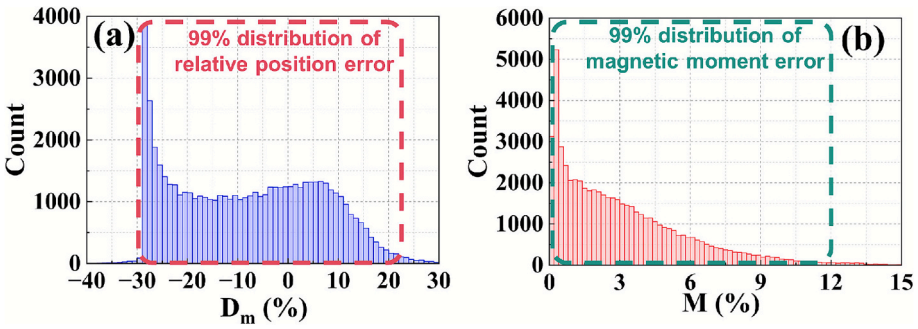

Fig. 6. The blue distribution chart represents the magnetic moment error, and the red distribution chart represents the positioning point error. (For interpretation of the references to colour in this figure legend, the reader is referred to the web version of this article.)

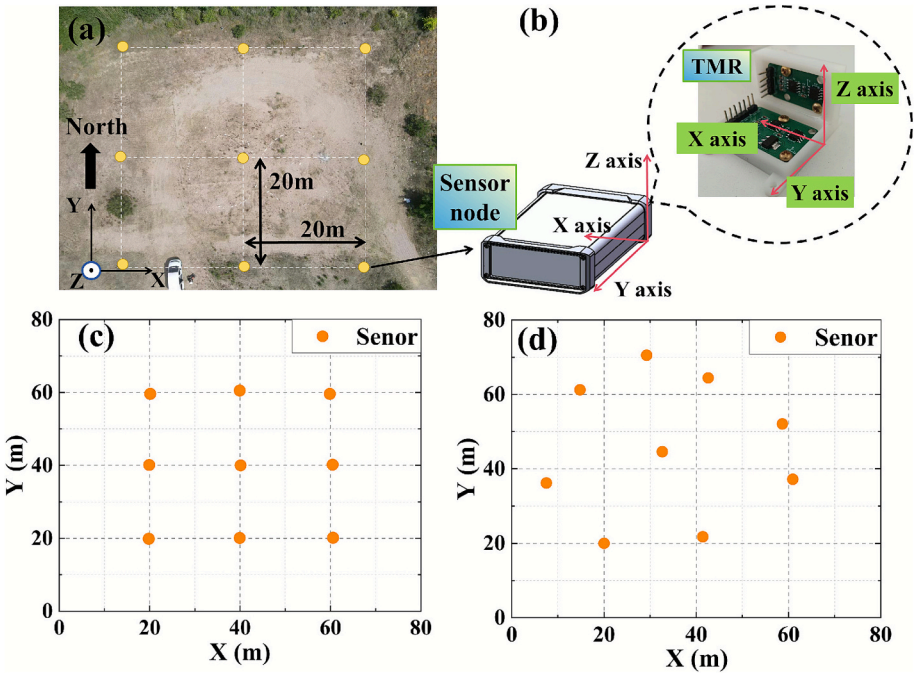

Fig. 7. (a) Picture of the experimental layout consisting of 9 sensors and one sensor as compensation for a 2 m (width)× 5.5 m (length) pickup truck moving in a 40 m × 40 m area; (b) Each sensor node is composed of three orthogonal TMR; (c) Schematic diagram of the sensing network distributed in a rectangular type according to a spacing of 20 m; and (d) Random distribution of the sensing network in a 40 m × 40 m area.

which is due to the fact that the Centroid Localization algorithm only starts with the relationship between the signal strength and the distance to the target and directly ignores information such as the magnetic moment of the vehicle.

The TFM only has good positioning effect in straight line movement, and when the vehicle has a fast steering, it will have a large error. The positioning errors of these three algorithms are counted separately, and the results are shown in Table 1 and Table 2. But it should be noted that there is a trajectory interruption for both regular placement and irregular placement conditions. In Fig. 9(a), for example, at the coordinate of X = 40 m, Y = 55 m, it almost loses the localization points. This issue is mainly due to the target located at the boundary of the sensor array. In fact, expanding the number of sensor nodes can effectively reduce this effect. Additionally, this issue can be also addressed by incorporating advanced signal processing and detection methods in future work, which can enhance detection capabilities under low signal-to-noise ratio conditions.

The travelling trajectory of the target vehicle in the sensor array was localized by using the Real-Time Kinematic (RTK) system, which has a localization error of less than 10 cm. So, this measured position is used for the real path of the vehicle, vehicles moved for 19 s in the regular array and 23 s in the irregular array. The results of localization trajectories are shown in Fig. 9(a), (b): The red curves indicate the trajectories localized by the GS-PSO algorithm and tracked by the ST-IMM filter, the green ones indicate the results obtained by the TFM algorithm, and the purple ones indicate the results obtained by the Centroid Localization algorithm. According to the trajectory, it can be found intuitively that the Centroid Localization algorithm has the lowest positioning accuracy, which is due to the fact that the Centroid Localization algorithm only starts with the relationship between the signal strength and the distance to the target and directly ignores information such as the magnetic moment of the vehicle. The TFM only has good positioning effect in straight line movement, and when the vehicle has a fast steering, it will have a large error. The positioning errors of these three algorithms are counted separately, and the results are shown in Table 1 and Table 2. But it should be noted that there is a trajectory interruption for both regular placement and irregular placement conditions.

In Fig. 9(a), for example, at the coordinate of X = 40 m, Y = 55 m, it almost loses the localization points. This issue is mainly due to the target located at the boundary of the sensor array. This is primarily because when the target approaches the array boundary, the number of sensors receiving signals with intensity exceeding the threshold fails to meet the

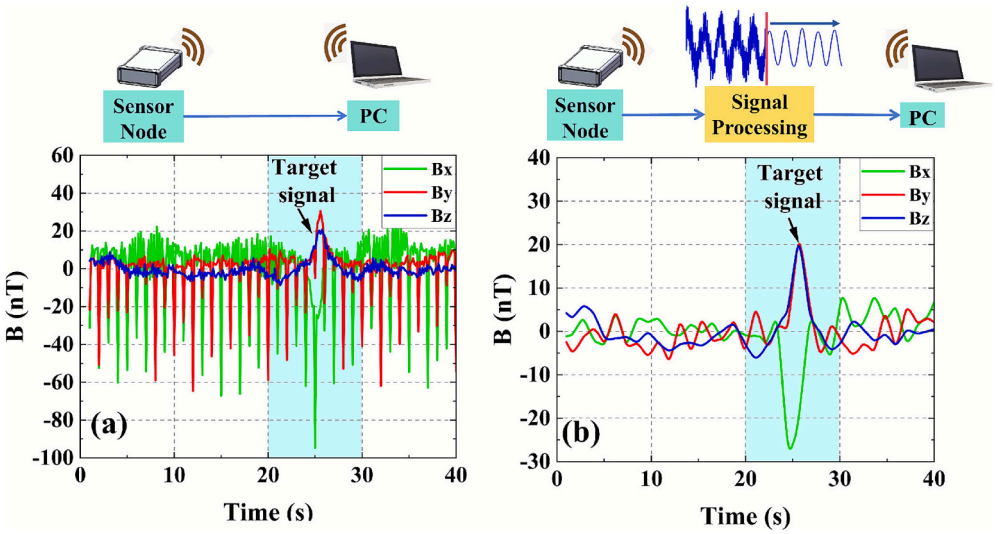

Fig. 8. (a) Raw data sent from the sensor to the computer. (b) Data after noise reduction processing.

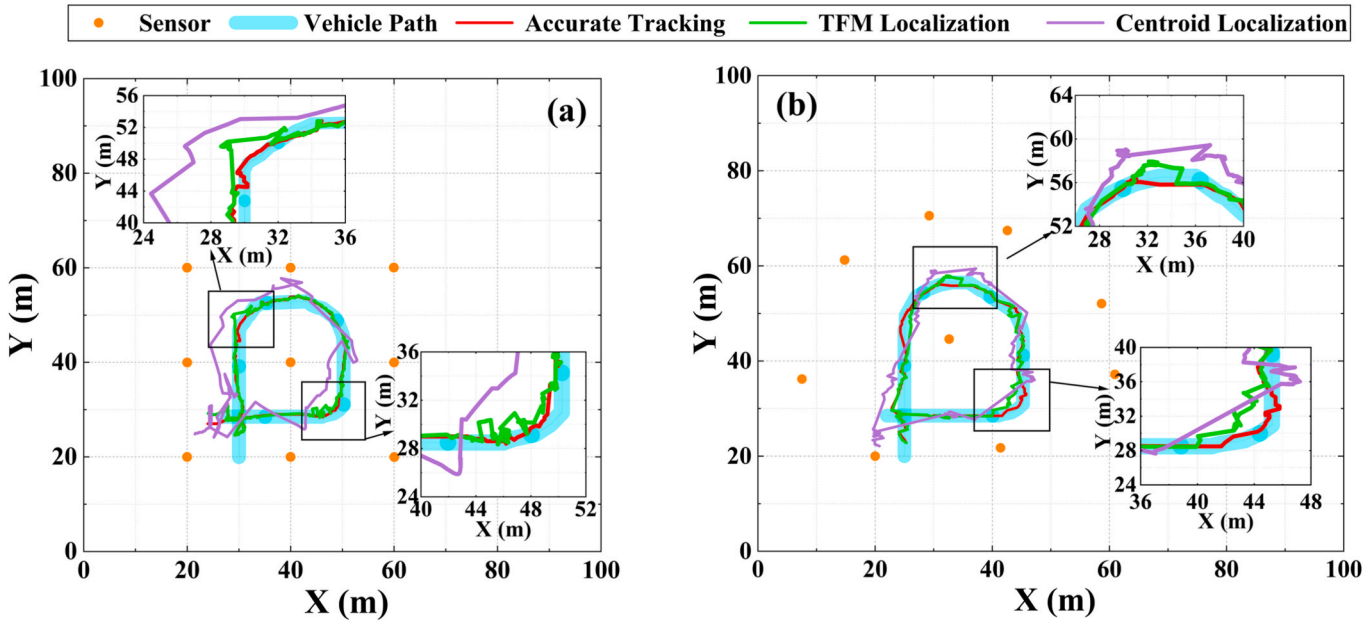

Fig. 9. Target tracking trajectories and error statistics under two distributions of sensor networks: (a) Rectangular distribution of sensor networks; (b) Random distribution layout of the sensing network.

Table 1
Comparison of localization results of the three algorithms under regular arrays.

Search method	M (%)	Time consumes(s)
Centroid Localization Algorithm [51]	27.38	20.32
TFM [32]	11.03	23.10
GS-PSO-ST-IMM*	6.30	20.4

Table 2
Comparison of localization results of the three algorithms under unregular arrays.

Search method	M (%)	Time consumes(s)
Centroid Localization Algorithm [51]	33.74	24.82
TFM [32]	11.86	26.30
GS-PSO-ST-IMM*	8.43	25.08

required count *N*. To mitigate this issue, expanding the array scale to enhance coverage serves as an effective measure. Additionally, adopting advanced signal processing and detection methods to replace threshold-based detection can improve detection capabilities under low signal-to-noise ratio (SNR) conditions, thereby addressing the trajectory loss problem at the array boundary.

Meanwhile, according to the running time of the vehicle and the positioning time of the algorithm, it is shown that our proposed GS-PSO-ST-IMM positioning and tracking algorithm process can locate the vehicle in real time, with a very small latency.

5. Conclusion

In this study, the GS-PSO-ST-IMM localization and tracking algorithm is proposed to solve the localization problem of nonlinear moving vehicles. Specifically, we introduce the geomagnetic background field to solve the target position and magnetic moment through a step-by-step

strategy of gradually refining the model. Furthermore, we improve the tracking effect of the vehicle under nonlinear motion by dynamically fusing multiple linear models and adjusting the filter gain factor according to the idea of strong tracking based on interactive multi-model filtering. According to the simulation and experimental results, our proposed localization algorithm has been demonstrated to improve the localization accuracy for the nonlinear moving target significantly compared with the traditional method. Moreover, the average positioning time is only about 2 s behind the real vehicle motion, which proves that our algorithm can also guarantee real-time performance.

CRediT authorship contribution statement

Chen Yang: Writing – original draft, Software, Resources, Methodology, Formal analysis, Data curation. **Junqi Gao:** Writing – review & editing, Visualization, Validation, Supervision, Conceptualization. **Chuancheng Tang:** Validation, Supervision, Data curation. **Xiangxiang Zhang:** Software, Data curation, Conceptualization. **Qiuwei Liu:** Visualization, Validation. **Lindong Pan:** Writing – review & editing, Data curation. **Ying Shen:** Writing – review & editing, Funding acquisition, Conceptualization.

Declaration of competing interest

The authors declare the following financial interests/personal relationships which may be considered as potential competing interests: Ying Shen reports financial support was provided by National Natural Science Foundation of China. Ying Shen reports financial support was provided by the Natural Science Foundation of Heilongjiang Province. Ying Shen reports a relationship with National Natural Science Foundation of China that includes: funding grants. If there are other authors, they declare that they have no known competing financial interests or personal relationships that could have appeared to influence the work reported in this paper.

Acknowledgements

This work was supported in part by the National High-Level Personnel of Special Support Program under Grant 006170130620, and in part by the Key Laboratory of Radio Wave Environment Characteristics and Modeling Technology Funding (No.JCKY2024210C 61424030202), and Qingdao Natural Science Foundation (25-1-1-61-zyyd-jch).

Data availability

The data that has been used is confidential.

References

[1] O.B. Sezer, E. Dogdu, A.M. Ozbayoglu, Context-aware computing, learning, and big data in internet of things: a survey, IEEE Internet Things J. 5 (2018) 1–27.
[2] A. Arora, P. Dutta, S. Bapat, V. Kulathumani, H. Zhang, V. Naik, V. Mittal, H. Cao, M. Demirbas, M. Gouda, Y. Choi, T. Herman, S. Kulkarni, U. Arumugam, M. Nesterenko, A. Vora, M. Miyashita, A line in the sand: a wireless sensor network for target detection, classification, and tracking, Comput. Netw. 46 (2004) 605–634.
[3] M. Pérez, J. Parras, S. Zazo, I.A.P. Álvarez, M.d.M.S. Lluch, Using a deep learning algorithm to improve the results obtained in the recognition of vessels size and trajectory patterns in shallow areas based on magnetic field measurements using fluxgate sensors, IEEE Trans. Intell. Transport. Syst. 23 (2022) 3472–3481.
[4] A. Agurto, Y. Li, G.Y. Tian, N. Bowring, S. Lockwood, A review of concealed weapon detection and research in perspective, 2007 IEEE Int. Conf. Network. Sens. Control (2007) 443–448.
[5] H. Jin, J. Guo, H. Wang, Z. Zhuang, J. Qin, T. Wang, Magnetic anomaly detection and localization using orthogonal basis of magnetic tensor contraction, IEEE Trans. Geosci. Remote Sens. 58 (2020) 5944–5954.
[6] S.D. Billings, Discrimination and classification of buried unexploded ordnance using magnetometry, IEEE Trans. Geosci. Remote Sens. 42 (2004) 1241–1251.
[7] Y. Wang, J. Chai, H. Wang, W. Cao, Y. Wang, L. Yue, J. Zhao, A novel 3D target location method using 2D orthonormal basis functions of total vertical gradient of magnetic anomaly, Measurement 253 (2025) 117457.
[8] J. Tarnawski, K. Buszman, M. Woloszyn, B. Puchalski, The influence of the geographic positioning system error on the quality of ship magnetic signature reproduction based on measurements in sea conditions, Measurement 229 (2024) 114405.
[9] P. Lin, N. Zhang, M. Chang, L. Xu, Research on the model and the location method of ship shaft-rate magnetic field based on rotating magnetic dipole, IEEE Access 8 (2020) 162999–163005.
[10] R. Berešík, J. Puttera, J. Kurty, J. Jurčo, Magnetic sensor system concept for ground vehicles detection, International Conference on Military Technologies (ICMT) 2017 (2017) 710–715.
[11] M. Erol-Kantarci, H.T. Mouftah, S. Oktug, A survey of architectures and localization techniques for underwater acoustic sensor networks, IEEE Communications Surveys & Tutorials 13 (2011) 487–502.
[12] A. Tingle, The coming 5G evolution in network centric warfare the sensor saturation theory, MitchellForum (2020) 1–11.
[13] P. Braca, R. Goldhahn, G. Ferri, K.D. LePage, Distributed information fusion in multistatic sensor networks for underwater surveillance, IEEE Sens. J. 16 (2016) 4003–4014.
[14] S. Kong, J. Sun, C. Qiu, Z. Wu, J. Yu, Extended state observer-based controller with model predictive governor for 3-D trajectory tracking of underactuated underwater vehicles, IEEE Trans. Ind. Inf. 17 (2021) 6114–6124.
[15] R. Sithiravel, B. Balaji, B. Nelson, M.K. McDonald, R. Tharmarasa, T. Kirubarajan, Airborne maritime surveillance using magnetic anomaly detection signature, IEEE Trans. Aerosp. Electron. Syst. 56 (2020) 3476–3490.
[16] Z.X. Tian, Underwater magnetic surveillance system for port protection, 2011 IEEE 2nd International Conference on Computing, Control and Industrial Engineering, 2011, pp. 282-285.
[17] M. Luo, Z. Xu, J. Pei, Z. Li, J. Chen, A tracking approach of a moving ferromagnetic object using triaxial search coil data, IEEE Trans. Geosci. Remote Sens. 62 (2024) 1–12.
[18] H.-M. Shen, C. Lian, X.-W. Wu, F. Bian, P. Yu, G. Yang, Full-pose estimation using inertial and magnetic sensor fusion in structurized magnetic field for hand motion tracking, Measurement 170 (2021) 108697.
[19] M. Birsan, Recursive Bayesian Method for magnetic Dipole Tracking with a Tensor Gradiometer, IEEE Trans. Magn. 47 (2011) 409–415.
[20] T. Nara, S. Suzuki, S. Ando, A closed-form formula for magnetic dipole localization by measurement of its magnetic field and spatial gradients, IEEE Trans. Magn. 42 (2006) 3291–3293.
[21] C. Wang, X. Zhang, X. Qu, X. Pan, G. Fang, L. Chen, A modified magnetic gradient contraction based method for ferromagnetic target localization, Sensors 16 (2016) 2168.
[22] B. Oruç, Location and depth estimation of point-dipole and line of dipoles using analytic signals of the magnetic gradient tensor and magnitude of vector components, J. Appl. Geophys. 70 (2010) 27–37.
[23] N. Yağmur, B.B. Alagöz, Comparision of solutions of numerical gradient descent method and continous time gradient descent dynamics and lyapunov stability, in: 2019 27th Signal Processing and Communications Applications Conference (SIU), IEEE, 2019, pp. 1-4.
[24] S. Hu, J. Wang, Z.-H. Huang, An inexact augmented Lagrangian multiplier method for solving quadratic complementary problems: an adapted algorithmic framework combining specific resolution techniques, J. Comput. Appl. Math. 361 (2019) 64–78.
[25] W. Xie, X. Zhang, Y. Mu, Y. Zheng, A subsurface targets' classification method utilizing gradient learning technique, IEEE Geosci. Remote Sens. Lett. 19 (2022) 1–5.
[26] Q. Huang, X. Zhang, J. Ma, Underground Magnetic Localization Method and Optimization Based on Simulated Annealing Algorithm, 2015 IEEE 12th Intl Conf on Ubiquitous Intelligence and Computing and 2015 IEEE 12th Intl Conf on Autonomic and Trusted Computing and 2015 IEEE 15th Intl Conf on Scalable Computing and Communications and Its Associated Workshops (UIC-ATC-ScalCom), 2015, pp. 168-173.
[27] L. Wang, T. Zhou, Q. Niu, Y. Hui, Z. Hou, A method and device for detecting the number of magnetic nanoparticles based on weak magnetic signal, Processes 7 (2019) 480.
[28] H. Xie, M. Sun, X. Fan, Z. Lin, W. Chen, L. Wang, L. Dong, Q. He, Reconfigurable magnetic microrobot swarm: multimode transformation, locomotion, and manipulation, Sci. Rob. 4 (2019) eaav8006.
[29] W.a. Yang, C. Hu, M.Q.-H. Meng, S. Song, H. Dai, A six-dimensional magnetic localization algorithm for a rectangular magnet objective based on a particle swarm optimizer, IEEE Trans. Magnet. 45 (2009) 3092–3099.
[30] G. Rossides, B. Metcalfe, A. Hunter, Particle swarm optimization—an adaptation for the control of robotic swarms, Robotics 10 (2021) 58.
[31] C.P. Du, M.Y. Xia, S.X. Huang, Z.H. Xu, X. Peng, H. Guo, Detection of a moving magnetic dipole target using multiple scalar magnetometers, IEEE Geosci. Remote Sens. Lett. 14 (2017) 1166–1170.
[32] J. Wang, J. Gao, S. Zhao, R. Zhu, Z. Jiang, Z. Chu, Z. Mao, Y. Shen, From model to algorithms: distributed magnetic sensor system for vehicle tracking, IEEE Trans. Ind. Inf. 19 (2023) 2963–2972.
[33] B.Z. Hu, M.C. Pan, P. Jiang, W.G. Tian, J.F. Hu, J.H. Hu, The research on magnetic target detection technology based on wireless sensor network, Appl. Mech. Mater. 644–650 (2014) 1213–1217.
[34] J. Ge, S. Wang, H. Dong, H. Liu, D. Zhou, S. Wu, W. Luo, J. Zhu, Z. Yuan, H. Zhang, Real-time detection of moving magnetic target using distributed scalar sensor

based on hybrid algorithm of particle swarm optimization and gauss–newton method, IEEE Sens. J. 20 (2020) 10717–10723.
[35] X. Zhang, X. Kang, X. Chen, H. Lv, Z. Geng, L. Fan, C. Kang, Measurement of far field magnetic moment vector of a moving ferromagnetic object, IEEE Sens. J. 20 (2020) 10903–10912.
[36] X. Zhang, L. Fan, P. Cheng, C. Chen, X. Liu, C. Kang, A method to remotely track a magnetic target using a scalar magnetometer array, J. Sens. 2017 (2017) 6510980.
[37] M. Birsan, Recursive Bayesian method for magnetic dipole tracking with a tensor gradiometer, IEEE Trans. Magn. 47 (2010) 409–415.
[38] Y. Sun, H. Wang, W. Quan, X. Ma, Z. Tao, M. Elhajj, W.Y. Ochieng, Smart road stud-empowered vehicle magnetic field distribution and vehicle detection, IEEE Trans. Intell. Transp. Syst. 24 (2023) 7357–7362.
[39] H. Zhang, W. Zhou, G. Liu, Z. Wang, Z. Qian, Fine-grained vehicle make and model recognition framework based on magnetic fingerprint, IEEE Trans. Intell. Transp. Syst. 25 (2024) 8460–8472.
[40] A. Amodio, M. Ermidoro, S.M. Savaresi, F. Previdi, Automatic vehicle model recognition and lateral position estimation based on magnetic sensors, IEEE Trans. Intell. Transp. Syst. 22 (2020) 2775–2785.
[41] N. Wahlström, F. Gustafsson, Magnetometer modeling and validation for tracking metallic targets, IEEE Trans. Signal Process. 62 (2014) 545–556.
[42] N. Wahlström, J. Callmer, F. Gustafsson, Single target tracking using vector magnetometers, 2011 IEEE International Conference on Acoustics, Speech and Signal Processing (ICASSP), 2011, pp. 4332-4335.
[43] Z. Xiaojun, F. Liming, C. Peng, C. Chunlei, L. Xuejun, K. Chong, A method to remotely track a magnetic target using a scalar magnetometer array, J. Sens. 2017 (2017) 1–9.
[44] L. Fan, C. Kang, X. Zhang, Q. Zheng, M. Wang, An efficient method for tracking a magnetic target using scalar magnetometer array, Springerplus 5 (2016) 502.
[45] H. Xiong, J. Tang, H. Xu, W. Zhang, Z. Du, A robust single GPS navigation and positioning algorithm based on strong tracking filtering, IEEE Sens. J. 18 (2018) 290–298.
[46] M. Kiani, R. Ahmadvand, The strong tracking innovation filter, IEEE Trans. Aerosp. Electron. Syst. 58 (2022) 3261–3270.
[47] J. Wang, Z. Jiang, J. Gao, S. Zhao, W. Zhai, Y. Shen, Frequency characteristics analysis for magnetic anomaly detection, IEEE Geosci. Remote Sens. Lett. 19 (2021) 1–5.
[48] Y. Guo, X. Zhou, J. Li, R. Ba, Z. Xu, S. Tu, L. Chai, A novel and optimized sine–cosine transform wavelet threshold denoising method based on the sym4 basis function and adaptive threshold related to noise intensity, Appl. Sci. 13 (2023) 10789.
[49] J. Gong, A study on wavelet selection in power signal denoising, IOP Conference Series: Earth and Environmental Science, IOP Publishing, 2021, pp. 012104.
[50] N. You, L. Han, D. Zhu, W. Song, Research on image denoising in edge detection based on wavelet transform, Appl. Sci. 13 (2023) 1837.
[51] B. Hu, M. Pan, P. Jiang, W. Tian, J. Hu, J. Hu, The Research on Magnetic Target Detection Technology Based on Wireless Sensor Network, International Conference on Machine Tool Technology and Mechatronics Engineering, 2014.